13th International Symposium on Turbulence and Shear Flow Phenomena (TSFP13)
Montreal, Canada, June 25–28, 2024

WALL-MODELED LES OF UNSTEADY AERODYNAMICS OVER A TRANSONIC PITCHING AIRFOIL AT HIGH REYNOLDS NUMBER

Hiromichi Sashida
Department of Aerospace Engeneering
Tohoku university
Sendai Miyagi 980-8579, Japan
hiromichi.sashida.t7@dc.tohoku.ac.jp

Shigetaka Kawai
Department of Aerospace Engeneering
Tohoku university
Sendai Miyagi 980-8579, Japan
shigetaka.kawai.a3@tohoku.ac.jp

Soshi Kawai
Department of Aerospace Engeneering
Tohoku university
Sendai Miyagi 980-8579, Japan
kawai@tohoku.ac.jp

ABSTRACT

This study conducts the wall-modeled large-eddy simulation (WMLES) of transonic flows ($Ma_\infty \simeq 0.8$) around a pitching NACA64A010 symmetrical airfoil at a high Reynolds number condition ($Re_c \simeq 1.2 \times 10^7$). The flow field around the pitching airfoil at mean angles of attack of $\alpha_m = 0^\circ$ and $\alpha_m = 4^\circ$ are simulated with the amplitude $\alpha_0 = 1.01^\circ$ and nondimensional frequency $k \simeq 0.2$. At $\alpha_m = 0^\circ$, the obtained data agree well with the experimental data, which shows the effectiveness of the WMLES for accurately capturing the phase difference. In the case of $\alpha_m = 4^\circ$, even though the flow field is accompanied by the flow separation, the WMLES reasonably predicts the unsteady aerodynamic forces. The predicted hysteresis of lift coefficient loops in the opposite direction between $\alpha_m = 0^\circ$ and 4° due to the contrary trend of shock motion over an airfoil. The results show that the existence of the flow separation distinctly affects the phase difference of unsteady aerodynamic forces. Finally, we evaluate the energy exchange between the flow and the pitching airfoil. The results show that the role of shock is negative damping at $\alpha_m = 0^\circ$ with attached flow and positive damping at $\alpha_m = 4^\circ$ with separated flow.

INTRODUCTION

Aeroelasticity phenomena, such as flutter, are caused by energy transfer from flow to structure. This can lead to the destruction of the structures, and the accurate prediction of flutter is crucial for aircraft design. In the transonic regime, the flutter boundary drops rapidly (which is called transonic dip), and the aeroelasticity phenomenon has become more vital as aircraft cruising speed has increased in recent years. One of the reasons for the transonic dip is the phase delay of the aerodynamic forces with shock against the oscillation of the structures (Isogai, 1979, 1981). Therefore, for more elucidation of the transonic flutter, it is important to accurately capture the phase difference of shock over pitching airfoils and the consequent energy exchange between the airfoil and flowfields. As a simple model of the flutter, analyses of flows around a forced pitching airfoil have often been conducted to verify the accuracy of the unsteady aerodynamic force predictions compared with the wind tunnel experiment (Davis and Malcolm, 1980; Oyeniran *et al*. 2022). Also in this study, we target an analysis of a pitching airfoil.

The transonic flow around an airfoil includes interactions between the shock wave and turbulent boundary layers, which may cause unsteady flow separation. Since such complex turbulent phenomena are crucial for aerodynamics over pitching airfoils, an unsteady high-fidelity simulation such as large-eddy simulation (LES) is effective for the prediction of flows over pitching airfoils. However, the wall-resolved LES is prohibited in terms of computational cost due to the high Reynolds number such as the real flight condition $Re_c \sim 10^7$. Thus, although LES of flows around a pitching airfoil has been considered to be effective for an accurate prediction of flutter, there have not been many such researches. To conduct high-fidelity simulation while reducing the cost, we adopt wall-modeled LES (WMLES) (Kawai and Larsson, 2012). Since the WMLES models the inner layer of the boundary layer, the WMLES can drastically reduce the computational costs and enable high-fidelity LES at high Reynolds numbers. In addition, as the WMLES does not resolve the inner-layer turbulence with a small time scale, the WMLES can take a larger time step size. For example, by employing WMLES, Fukushima and Kawai (Fukushima and Kawai, 2018) successfully reproduced the transonic buffet which is an unsteady phenomenon with a long timescale, and suggest the potential of WMLES to predict the unsteady aerodynamics over an airfoil even when there is separation of the flow.

In this study, we conduct the WMLES of the transonic flow ($Ma_\infty \simeq 0.8$) around a pitching airfoil at high Reynolds number ($Re_c \simeq 1.2 \times 10^7$). By comparing the results with the experimental results (Davis and Malcolm, 1980), we validate the prediction accuracy of the WMLES on moving grids. In addition, we evaluate the energy exchange between the airfoil and flow and discuss the system instability under the present conditions.

PROBLEM SETTINGS

This study simulates the flow around a NACA64A010 symmetrical airfoil. The settings are referring to the wind tunnel experiment (Davis and Malcolm, 1980). The pitching center is set to 25 % chord length. The non-dimensional frequency is defined as $k = \omega c/(2U_\infty)$, where ω, c, and U_∞ are angular frequency, chord length, and the freestream velocity, respectively. The angle of attack is forced to oscillate according to the following equation:

$$\alpha(t) = \alpha_m + \alpha_0 \sin(2kMa_\infty t). \tag{1}$$

In this study, we simulate two cases of the mean angles of attack of $\alpha_m = 0^\circ$ and 4°. The flowfield is attached under the former condition and largely separated under the latter condition. The freestream Mach number, chord-based Reynolds number, and non-dimensional frequency are set to $Ma_\infty \simeq 0.8$, $Re_c \simeq 1.2 \times 10^7$, and $k \simeq 0.2$, respectively.

NUMERICAL METHODS

The spatially-filtered compressible Navier–Stokes equations are solved in LES. The spatial derivatives are evaluated by the sixth-order compact difference scheme (Lele, 1992) with the eighth-order low-pass filter (Lele, 1992; Gaitonde and Visbal, 2000). The localized artificial diffusivity (LAD) method (Kawai *et al*., 2010) is employed to robustly capture the shock waves. The selective mixed-scale model (Lenormand *et al*., 2000) is used to compute the SGS turbulent viscosity. The third-order TVD Runge–Kutta scheme is used for time integration.

In this study, we employ the equilibrium wall model (Kawai and Larsson, 2012). In this wall model, the unresolved inner layer is modeled by solving the following two coupled ordinary differential equations, which are derived from the streamwise momentum and total energy equations under the equilibrium boundary layer approximation.

$$\frac{d}{dy}\left[(\mu + \mu_{t,\mathrm{wm}})\frac{dU_{||}}{dy}\right] = 0 \tag{2}$$

$$\frac{d}{dy}\left[(\mu + \mu_{t,\mathrm{wm}})U_{||}\frac{dU_{||}}{dy} + c_p\left(\frac{\mu}{Pr} + \frac{\mu_{t,\mathrm{wm}}}{Pr_t}\right)\frac{dT}{dy}\right] = 0 \tag{3}$$

where y is the wall-normal direction, $U_{||}$ is the wall-parallel velocity, T is the temperature and c_p is the specific heat at constant pressure. $Pr_t (= 0.9)$ is the turbulent Prandtl number. The wall model receives physical quantities at a matching point located in the inner layer ($y = h_{\mathrm{wm}}$) from the LES grid as input and predicts wall shear stress and wall heat flux by solving the above two equations, which are then fed back to the LES as the boundary conditions. Based on the prior study (Kawai and Larsson, 2012), the matching point is set to the fifth grid point from the wall in the LES domain ($h_{\mathrm{wm}} = y_5$). The mixing-length eddy-viscosity model with van Driest damping is employed to determine $\mu_{t,\mathrm{wm}}$ in the wall model:

$$\mu_{t,\mathrm{wm}} = \kappa \rho y \sqrt{\frac{\tau_w}{\rho}} D \tag{4}$$

$$D = \left[1 - \exp\left(-\frac{y^+}{A^+}\right)\right]^2 \tag{5}$$

where $y^+ = \rho_w u_\tau y/\mu_w$, $u_\tau = \sqrt{\tau_w/\rho_w}$ (the subscript w means the value of the physical quantity at the wall surface), $\kappa =$ 0.41, and $A^+ = 17$. In this study, the wall-modeled LES switches between laminar and turbulent flows by setting $\mu_t = 0$ in the upstream region of $x/c = 0.05$, which is the transition point in the wind tunnel experiment (Davis and Malcolm, 1980). At the wall, an adiabatic non-slip condition is employed.

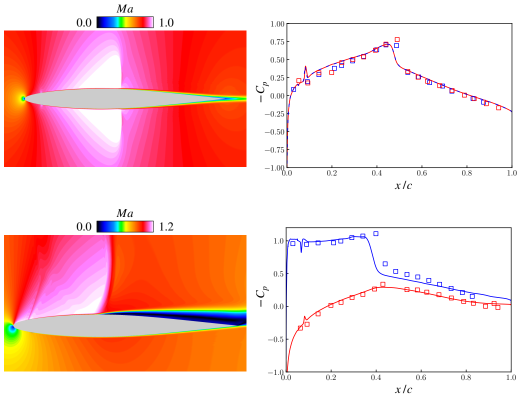

Figure 1: Distributions of time-averaged Mach number (left) and surface pressure coefficient (right) at $\alpha = 0^\circ$ (top) and $\alpha = 4^\circ$ (bottom) for static airfoil. Square, Exp. (Davis and Malcolm, 1980); line, WMLES. Blue, upper surface; red, lower surface.

The C-type grid is used in this study. The outer boundary is set at a distance of $100c$ from the airfoil, and the span length is set to $7.590\%c$. The grid spacings are $\delta/\Delta x \simeq \delta/\Delta y \simeq \delta/\Delta z \simeq 25$ based on the boundary layer thickness δ at 20% chord position, which is confirmed to be sufficient for flat-plate turbulent boundary layer by a previous study (Kawai and Larsson, 2012). The total number of grid points is approximately 3.7 billion (with 10,811 grid points in the chord direction, 498 points in the wall-normal direction, and 694 points in the span direction). The shown results by WMLES in this paper are spanwise averaged.

RESULTS

Static airfoil

Figure 1 shows the time- and spanwise-averaged Mach number and surface pressure coefficient distributions for the static airfoil at $\alpha = 0^\circ$ and 4°. In the case of $\alpha = 0^\circ$, shock waves exist symmetrically with respect to the airfoil. On the other hand, under the condition of $\alpha = 4^\circ$, there is a shock wave only on the upper surface, and the boundary layer is largely separated from the foot of the shock. The predicted surface C_p distributions by the WMLES are in good agreement with that of the wind tunnel, even at the high Reynolds number condition $Re_c \simeq 1.2 \times 10^7$ and in the presence of drastic separation. These results show the capability of the present WMLES to predict the complex and unsteady phenomena over an airfoil.

Pitching airfoil

In this section, we verify whether the WMLES can accurately capture the unsteady aerodynamic phenomena and the phase differences over a pitching airfoil. The time average and RMS of the surface pressure coefficient ($-C_p^{\mathrm{ave}} = -\overline{C_p}$ and $C_p^{\mathrm{RMS}} = \sqrt{\overline{C_p' C_p'}}/\alpha_0$) at $\alpha_m = 0^\circ$ are shown in Fig. 2. From Fig. 2b, we see that the shock motion range is about $0.4 <$

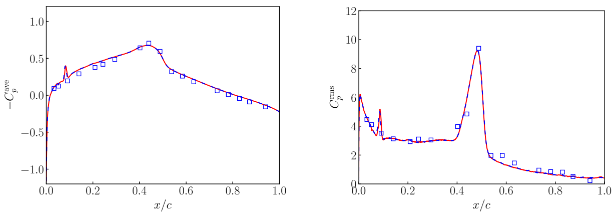

(a) Time-averaged C_p (b) RMS of C_p

Figure 2: Distributions of the time-averaged C_p and RMS of C_p at $\alpha_m = 0°$. Square, Exp. (Davis and Malcolm, 1980); line, WMLES. Blue, upper surface; red, lower surface.

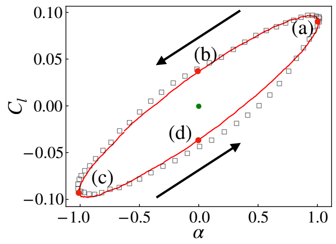

Figure 3: Time history of C_l at $\alpha_m = 0°$. Square, Exp (pitching airfoil) (Davis and Malcolm, 1980).; red, WMLES (pitching airfoil); green circle, WMLES (static airfoil). (a), maximum AoA; (b), mean AoA at pitch-down phase; (c), minimum AoA; (d), mean AoA at pitch-up phase.

$x/c < 0.5$. Also, the predicted distributions are in good agreement with the experimental data and show that the present WMLES successfully captures the aerodynamic phenomena over a pitching airfoil. Next, we compare the time history of unsteady aerodynamic force. Figure 3 shows the angles of attack versus lift coefficient during the cycle at $\alpha_m = 0°$. The lift coefficient makes a hysteresis loop in counterclockwise direction due to the phase difference between airfoil motion and aerodynamic forces. To see the relationship between the instantaneous lift coefficient and the flowfield at each time, the instantaneous Mach number distributions and surface pressure coefficient during the cycle at mean angles of attack $\alpha_m = 0°$ are shown in Fig. 4. First, taking a look at the mean angle of attack at the pitch-down phase (Fig. 4b), the shock on the upper surface is stronger and located more downstream than the shock on the lower surface, which causes the pressure difference between the upper and lower surface, and the lift force increases compared with the static case (Fig. 1). On the contrary, at the pitch-up phase (Fig. 4d), the behaviors of shocks on the upper and lower surfaces are opposite to those at pitch-down phase and thus the lift force decreases compared with the static case. Therefore, the hysteresis of lift draws the loop in the counterclockwise direction.

From here, the case where flow separation occurs is demonstrated. Figure. 5 shows the time average and RMS of the C_p at $\alpha_m = 4°$. The time-averaged pressure distributions forward and backward of the shock are in good agreement with the wind tunnel test. Figure 5b shows that although the predicted forward shock location differs slightly from the experiment, the maximum magnitude of the pressure in the range of shock motion agrees well. This indicates that the WMLES

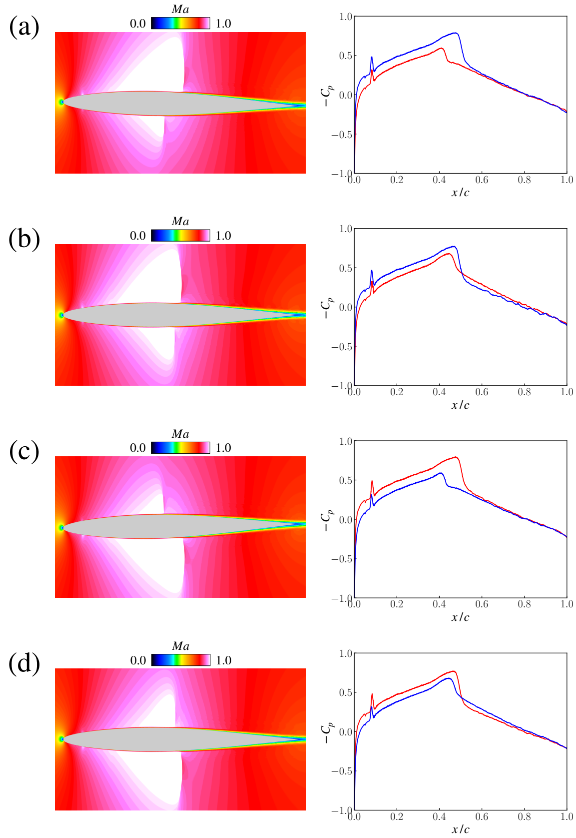

Figure 4: Distributions of Mach number (left) and surface pressure coefficient (right) during the cycle at $\alpha_m = 0°$. Blue, upper surface; red, lower surface. (a) maximum AoA, (b) mean AoA at pitch-down phase, (c) minimum AoA (d) mean AoA at pitch-up phase.

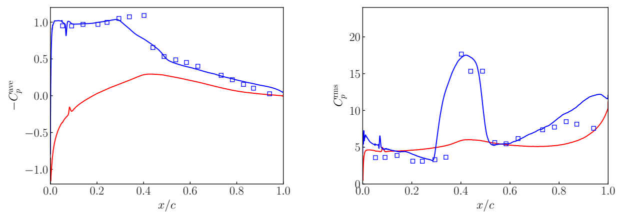

(a) Time-averaged C_p (b) RMS of C_p

Figure 5: Distributions of the time-averaged C_p and RMS of C_p at $\alpha_m = 4°$. Square, Exp. (Davis and Malcolm, 1980); solid line, WMLES. Blue, upper surface; red, lower surface.

well captures the shock motion. In Fig. 6, the hysteresis of the lift coefficient is observed similarly to the case of $\alpha_m = 0°$. However, the loop direction is clockwise, which is the reverse of that of $\alpha_m = 0°$. Figure 7 shows the instantaneous flowfield and the surface pressure coefficient. The shock location and the size of the separation of flow largely change with the airfoil motion. At the pitch-down phase (Fig. 7b) the shock wave on the upper surface exists more upstream and the lift decreases compared to the static case (Fig. 1), while at the phase of pitching down (Fig. 7d) the shock is located more downstream and the lift increases. These behaviors are opposite to $\alpha_m = 0°$, thereby leading to the opposite loop of the hysteresis. Also,

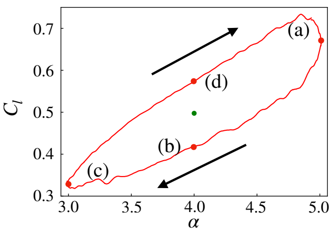

Figure 6: Time history of C_l at $\alpha_m = 4°$. Red, WMLES (pitching airfoil); green circle, WMLES (static airfoil). (a), maximum AoA; (b), pitch-down phase; (c), minimum AoA; (d), pitch-up phase.

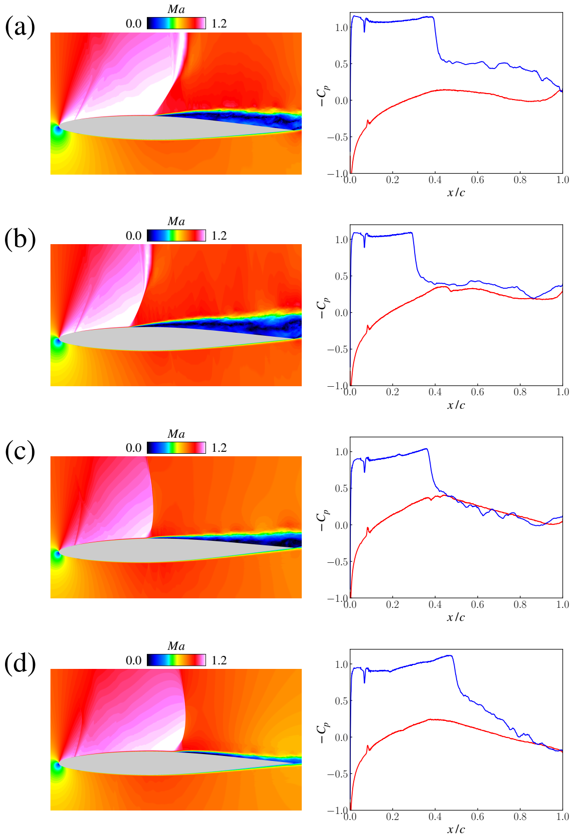

Figure 7: Distributions of Mach number (left) and surface pressure coefficient (right) during the cycle at $\alpha_m = 4°$. Blue, upper surface; red, lower surface. (a), maximum AoA; (b), mean AoA at pitch-down phase; (c), minimum AoA; (d), mean AoA at pitch-up phase.

this result suggests that the presence of separation affects the shock motion.

In order to quantify the phase difference in the time variation of the aerodynamic forces, we describe the time variation of the surface pressure coefficient C_p using the complex Fourier series:

$$-C_p(t) = \sum_{n=-\infty}^{\infty} c_n e^{in\omega t} \tag{6}$$

The real and imaginary parts of C_p used in this study are de-

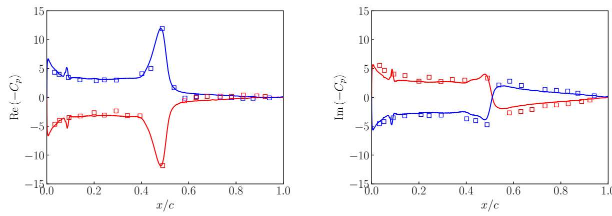

(a) Real part ($\alpha_m = 0°$) (b) Imaginary part ($\alpha_m = 0°$)

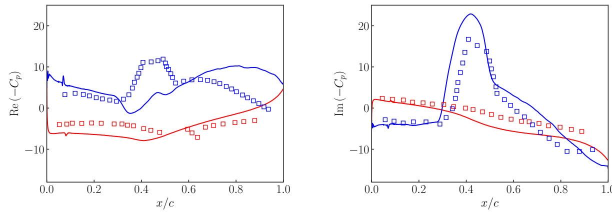

(c) Real part ($\alpha_m = 4°$) (d) Imaginary part ($\alpha_m = 4°$)

Figure 8: Distributions of the real and imaginary parts of C_p. Square, Exp. (Davis and Malcolm, 1980); solid line, WMLES. Blue, upper surface; red, lower surface.

fined using the first Fourier mode as

$$\mathrm{Re}(-C_p) \equiv \frac{2\mathrm{Re}(c_1)}{\alpha_0}\frac{180}{\pi}, \ \mathrm{Im}(-C_p) \equiv \frac{2\mathrm{Im}(c_1)}{\alpha_0}\frac{180}{\pi} \tag{7}$$

In physical meaning, the real and imaginary parts correspond to the time variation components of C_p in phase and $\pi/2$ out of phase, respectively, with the oscillation of the angle of attack. In terms of energy exchange, the out-of-phase component leads to energy extraction, and thus the accurate prediction of this out-of-phase component is particularly important.

The distributions of real and imaginary parts of the pressure coefficient are shown in Fig. 8. At $\alpha_m = 0°$, the obtained data agree well with those of the wind tunnel test in both real and imaginary parts. In the case of $\alpha_m = 4°$, the predicted real part shows a somewhat different trend and we are considering the details of these results now. Regarding the imaginary part, which is an important component for energy transfer of the airfoil, the WMLES reasonably predicts the distributions even though there is an unsteady large separation over an airfoil. These results suggest the capability of the WMLES to accurately predict the phase difference of aerodynamic forces and the resulting energy transfer.

Energy transfer over a pitching airfoil

Next we evaluate the energy exchange between the flow and the pitching airfoil. The energy transfer from fluid into an airfoil over a cycle is obtained by

$$\begin{aligned} E = \oint C_m \mathrm{d}\alpha &= \int_t^{t+T} C_m \frac{\mathrm{d}\alpha}{\mathrm{d}t}\mathrm{d}t \\ &= \int_t^{t+T} C_w \mathrm{d}t \end{aligned} \tag{8}$$

where C_m, t and T are the pitching moment coefficient, nondimensional time and period of pitching motion, respectively. The moment in the pitch-up direction is defined as positive.

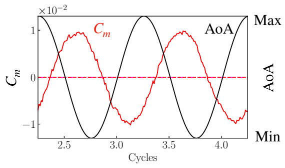

(a) $C_m(t)$ ($\alpha_m = 0°$)

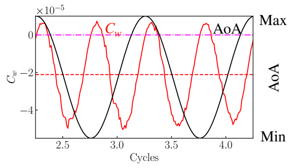

(b) $C_w(t)$ ($\alpha_m = 0°$)

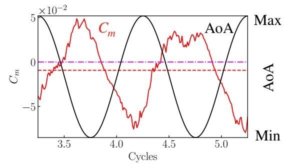

(c) $C_m(t)$ ($\alpha_m = 4°$)

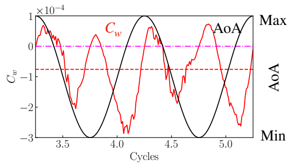

(d) $C_w(t)$ ($\alpha_m = 4°$)

Figure 9: Time history of C_m, C_w. Solid red line, time variation of each value; dashed red line, time averaged value; magenta dash-dot line, C_m or $C_w = 0$; black solid line, AoA.

C_w denotes the power coefficient determined by

$$C_w := C_m \frac{\mathrm{d}\alpha}{\mathrm{d}t} \tag{9}$$

When $C_w(t) > 0$, the energy is extracted by airfoil. By evaluating the power coefficient, we can quantify the energy transfer from the flow to the airfoil.

Figure 9 shows the time history of the pitching moment coefficient and power coefficient; the horizontal axis shows the cycles of pitching motion from $t = 0$ in Eq. (1). In both cases, the pitching moment shows the phase delay against the pitching motion. Also, although energy extraction occurs immediately after maximum and minimum angles of attack (note that when the angles of attack are maximum or minimum, the energy extraction is zero since $\mathrm{d}\alpha/\mathrm{d}t = 0$), the time averages of C_w during cycles are negative, which means that the total energy over a cycle transfers from the airfoil to flow in both cases.

In order to visualize the time-averaged local energy exchange over an airfoil, the distributions of the time-averaged power coefficient are shown in Fig. 10. Note that since the pitching center is located at $x/c = 0.25$, at which the pitching moment C_m is always zero, the energy exchange does not occur at this point. At the mean angle of attack $\alpha_m = 0°$, as the flow field is symmetry on the upper and lower surfaces, the C_w distributions on the upper and lower surfaces show the same trend: the energy extraction in the range of shock motion is positive while the energy extraction in the region behind the shock is negative. This suggests that the primary role of shock is negative damping against airfoil motion and the region behind the shock has a positive damping effect. On the contrary, at the condition of $\alpha_m = 4°$ with large flow separation, the trend largely changes. On the upper surface, where there exists a shock and large separation, the energy extraction is negative in the shock-motion range and gradually increases toward the trailing edge. On the lower surface, the energy extraction distributions show nearly zero in the range $0.0 < x/c < 0.4$ and then gradually decrease towards the trailing edge. Overall, the total energy extraction in the shock motion region is negative and changes to positive values near the trailing edge.

Finally, the time history of the spacial distributions of the surface pressure coefficient, moment coefficient and power coefficient are investigated in order to discuss the energy exchange related to shock in more detail. Figure 11 shows the result of $\alpha_m = 0°$. The negative C_p represents the suction and the positive C_m and C_w represent the pitch-up moment and energy transfer from the flow to the airfoil. The horizontal axis shows x/c and the vertical axis shows the cycles, or time. The texts "Down" ("Up") on right in the figures means that the phase is pitch-down (pitch-up). As indicated by arrows in Fig. 11, the discontinuities due to the shocks are observed at $x/c \simeq 0.5$ on both upper and lower surfaces. As seen from C_p in Fig. 11 a and b, near the shock, the pressure is low, i.e., the suction occurs on both surfaces, which causes the negative moment on the upper surface and the positive moment on the lower surface, respectively. As a result, near the shock, the energy is extracted at the pitch-down phases on the upper surface (Fig. 11a, C_w) and at the pitch-up phases on lower surfaces (Fig. 11b, C_w). In addition, the C_p map in Fig. 11a shows that the time in which the shock on the upper surface is located most downstream from the pitching center is slightly after the maximum angle of attack. Thus, the largest negative moment resulting from the shock occurs slightly after the maximum angle of attack, i.e., at the pitch-down phase as shown in C_m map in Fig. 11a. Since the negative moment at the pith-down phase causes the energy transfer from flow to the airfoil, the total energy extracted by the upper surface over a pitching cycle is positive (Fig. 10a and C_w in Fig. 11a). Also on the lower surface, the largest positive moment near the shock exists slightly after the minimum angle of attack at the pitch-up phase, which leads to the energy extraction by the airfoil.

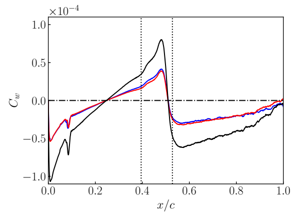

(a) $\alpha_m = 0°$

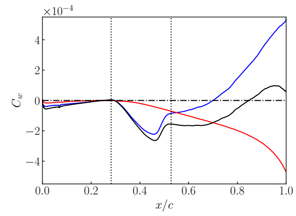

(b) $\alpha_m = 4°$

Figure 10: Time average of $C_w(x)$ distributions. Blue, upper surface; red, lower surface; black, sum of upper and lower surface. Dotted vertical line, the shock motion range determined by the C_p^{RMS}.

In the case of $\alpha_m = 4°$, the time history of the spacial distributions are shown in Fig. 12. Since the shock exists only on the upper surface, the discontinuity of the surface pressure coefficient is observed on the upper surface (C_p in Fig. 12a). Focusing on the upper surface, at the pitch-up phase, the moment near the shock is relatively large negative similar to $\alpha_m = 0°$ case. However, during the pitch-down phase, at which the negative moment leads to energy extraction, the shock is near the pitching center and the energy extraction related to the shock is small as shown in C_w map in Fig. 12a. Therefore, the energy transfers from the airfoil to flow in the range of the shock motion on the upper surface, which is consistent with the result in Fig. 10b.

CONCLUSIONS

We conduct the wall-modeled LES (WMLES) of transonic flow ($Ma_\infty \simeq 0.8$) over a pitching airfoil at a high Reynolds number ($Re_c \simeq 1.2 \times 10^7$) with mean angles of attack $\alpha_m = 0°$ and $4°$. The flowfield is attached at $\alpha_m = 0°$

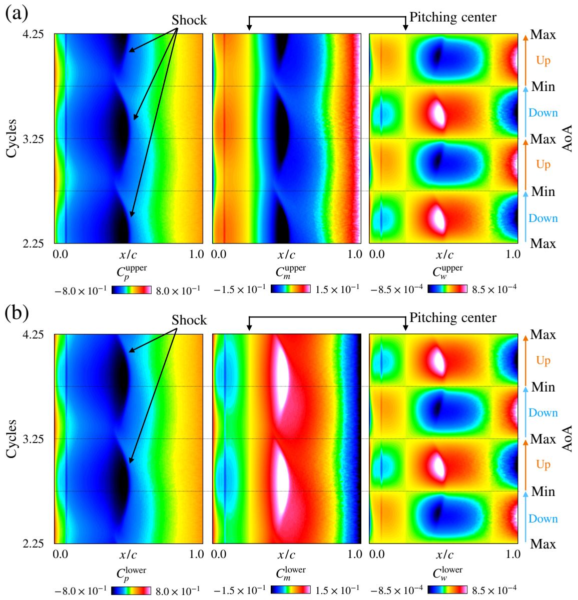

Figure 11: Time history of the spacial distributions of surface C_p, C_m, C_w at $\alpha_m = 0^\circ$ over the latest two cycles. (a) upper surface, (b) lower surface.

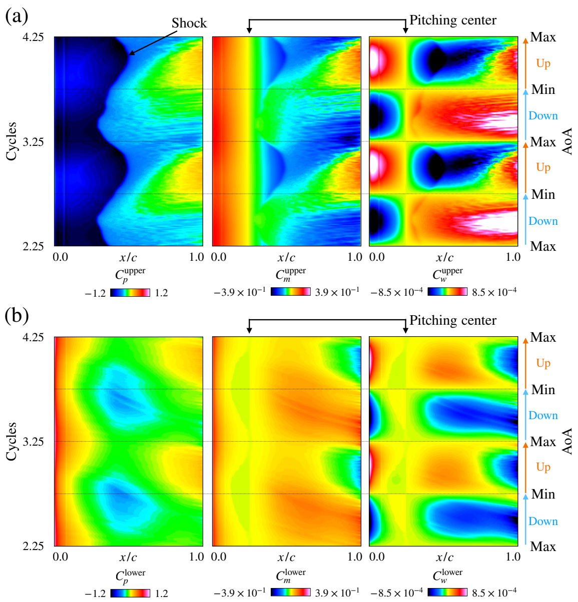

Figure 12: Time history of the spacial distributions of surface C_p, C_m, C_w at $\alpha_m = 4^\circ$ over the latest two cycles. (a) upper surface, (b) lower surface.

and large separation is observed at $\alpha_m = 4^\circ$. The WMLES well predicts the hysteresis of the lift coefficient. The loop direction at $\alpha_m = 4^\circ$ is the reverse of that of $\alpha_m = 0^\circ$ since the trend of shock motion is opposite, which suggests that the flow separation affects the behavior of shock. The predicted real (in phase) and imaginary ($\pi/2$ out of phase) components of time variation of pressure are reasonably in good agreement with those in the wind tunnel test. Since the phase difference causes the energy transfer, this result shows the effectiveness of the WMLES for accurately predicting the energy exchange. Finally, we quantify the energy exchange between the pitching airfoil and the flow field. The results show that the role of shock is negative damping at $\alpha_m = 0^\circ$ with the attached flow and positive damping at $\alpha_m = 4^\circ$ with the separated flow, which implies that the shock motion affected by the separation distinctly changes the trend of energy transfer compared to the case of the shock without separation.

In future work, we will investigate in more detail the role of flow separation in shock motion and energy transfer.

ACKNOWLEDGEMENTS

This work was supported in part by MEXT as "Program for Promoting Researches on the Supercomputer Fugaku" (Research toward DX in aircraft development led by digital flight, JPMXP1020230320) and the Japan Society for the Promotion of Science KAKENHI Grant Number 21H01523. This work used computational resources of supercomputer Fugaku provided by the RIKEN Center for Computational Science (Project ID: hp220160, hp230197, hp240203).

REFERENCES

Davis, S. S. & Malcolm, G.N. 1980 Transonic shock-wave/boundary-layer interactions on an oscillating airfoil. *AIAA Journal* **18** (11), 1306–1312.

Fukushima, Y. & Kawai, S. 2018 Wall-modeled large-eddy simulation of transonic airfoil buffet at high reynolds number. *AIAA Journal* **56** (6), 2372–2388.

Gaitonde, D. V. & Visbal, M. R. 2000 Pade-plusmn;-type higher-order boundary filters for the navier-stokes equations. *AIAA Journal* **38** (11), 2103–2112.

Isogai, Koji 1979 On the transonic-dip mechanism of flutter of a sweptback wing. *AIAA Journal* **17** (7), 793–795.

Isogai, Koji 1981 Transonic dip mechanism of flutter of a sweptback wing. ii. *AIAA Journal* **19** (9), 1240–1242.

Kawai, S. & Larsson, J. 2012 Wall-modeling in large eddy simulation: Length scales, grid resolution, and accuracy. *Physics of Fluids* **24** (1), 015105.

Kawai, S. & Lele, S. K. 2008 Localized artificial diffusivity scheme for discontinuity capturing on curvilinear meshes. *Journal of Computational Physics* **227** (22), 9498–9526.

Lele, S. K. 1992 Compact finite difference schemes with spectral-like resolution. *Journal of Computational Physics* **103** (1), 16–42.

Lenormand, E., Sagaut, P., Phuoc, L. T. & Comte, P. 2000 Subgrid-scale models for large-eddy simulations of compressible wall bounded flows. *AIAA Journal* **38** (8), 1340–1350.

Oyeniran, N.D., Miyake, T., Terashima, H., Seki, R., Ishiko, K. & Nonomura, T. 2022 Unsteady aerodynamics around a pitching airfoil with shock and shock-induced boundary-layer separation. *AIAA Journal* **60** (12), 6557–6565.